Composites Part B 268 (2024) 111052

Contents lists available at ScienceDirect

Composites Part B

journal homepage: www.elsevier.com/locate/compositesb

Metal matrix composite with superior ductility at 800 °C: 3D printed In718+ZrB_2 by laser powder bed fusion

Emre Tekoğlu [a,1], Alexander D. O'Brien [a,1], Jong-Soo Bae [b,1], Kwang-Hyeok Lim [b], Jian Liu [c], Sina Kavak [d], Yong Zhang [g], So Yeon Kim [e], Duygu Ağaoğulları [d], Wen Chen [c], A. John Hart [f], Gi-Dong Sim [b,**], Ju Li [a,e,*]

[a] Department of Nuclear Science and Engineering, Massachusetts Institute of Technology, Cambridge, 02139, USA
[b] Department of Mechanical Engineering, Korea Advanced Institute of Science and Technology, 291 Daehak-ro, Daejeon, Yuseong-gu, 34141, Republic of Korea
[c] Department of Mechanical and Industrial Engineering, University of Massachusetts, Amherst, 01003, USA
[d] Particulate Materials Laboratories, Metallurgical and Materials Engineering Department, Istanbul Technical University, Maslak, Istanbul, 34469, Turkey
[e] Department of Materials Science and Engineering, Massachusetts Institute of Technology, Cambridge, 02139, USA
[f] Department of Mechanical Engineering, Massachusetts Institute of Technology, Cambridge, 02139, USA
[g] Characterization.Nano, Massachusetts Institute of Technology, Cambridge, MA 02139, USA

ARTICLE INFO

Handling Editor: Dr Hao Wang

Keywords:
Laser powder bed fusion
Ni-based superalloy
Additive manufacturing
Mechanical property
In-situ alloying

ABSTRACT

We investigated the microstructure and mechanical properties of ZrB_2 fortified Inconel 718 (In718+ZrB_2) superalloy metal matrix composite (MMC), which was produced via Laser Powder Bed Fusion (LPBF). 2 vol% ZrB_2 nano powders (below 100 nm in diameter) were decorated on the surfaces of Inconel 718 alloy powders by high-speed blender. Microstructural analysis of the as-printed specimens showed that the ZrB_2 decomposed during LPBF, which promoted the formation of homogeneously distributed (Zr, Ni)-based intermetallic and (Nb, Mo, Cr)-based boride nanoparticles in the matrix. The 3D printed In718+ZrB_2 has remarkably lower porosity and smaller grain size compared to 3D printed In718 fabricated under the same LPBF conditions. The mechanical performance of the as-printed and heat-treated In718+ZrB_2 showed significantly higher room temperature (RT) hardness, RT yield strength (σ_{YS}), and RT ultimate tensile strength (σ_{UTS}) compared to In718. High-temperature tensile tests at 800 °C showed that In718+ZrB_2 has ~10 times higher tensile ductility with higher σ_{YS} (by 10 %) and σ_{UTS} (by 8 %) than pure In718.

1. Introduction

Ni-based superalloys are advanced engineering materials widely used in aerospace, marine, energy, and nuclear industries due to their exceptional high-temperature strength, corrosion, and oxidation resistance in harsh environments. Of these, Inconel 718 (In718), a Ni–Cr–Fe based superalloy, has found widespread use in aircraft engines and gas turbines owing to its superior mechanical stability and corrosion resistance at elevated temperatures up to 650–700 °C [1–3]. Despite the excellent historic performance of materials like In718, however, the recent push for cleaner energy has driven significant efforts for the design of more efficient power generation systems, in turn creating a strong demand for enhanced materials that will be able to accommodate even harsher working conditions. One option to meet such a need may be by forming composite structures with ceramic particulate reinforcements, commonly referred to as metal matrix composites (MMCs). Through utilizing harder, stiffer ceramic particle additions, these MMCs have achieved improvements in mechanical properties, physical properties, corrosion resistance, and more [4,5]. Conventionally, MMCs are produced via casting and powder metallurgy (PM) methods. MMCs prepared through casting processes show poor wettability of the ceramic nano-fillers and inhomogeneous distribution in the liquid metal matrix [6,7]. On the other hand, PM processes involve ball milling for mixing, diffusion, and sintering for consolidation [8]. Although this method can produce homogeneous components with good properties, it is also a time-consuming and expensive process.

* Corresponding author. Department of Nuclear Science and Engineering, Massachusetts Institute of Technology, Cambridge, 02139, USA.
** Corresponding author.
E-mail addresses: gdsim@kaist.ac.kr (G.-D. Sim), liju@mit.edu (J. Li).
[1] These authors contributed equally.

https://doi.org/10.1016/j.compositesb.2023.111052
Received 17 April 2023; Received in revised form 9 October 2023; Accepted 14 October 2023
Available online 16 October 2023

Furthermore, PM is severely limited in geometry and scalability, making it inadequate for producing complex industrial parts with near-net shapes [9].

Recently, additive manufacturing technologies (AM) have been implemented to produce metallic materials. Laser powder bed fusion (LPBF) especially has gained significant interest due to certain advantages compared to conventional manufacturing and other AM techniques (i.e., higher part complexity with higher resolution, lower powder cost) [10–12]. Some of the advantages compared to the conventional methods include reduction of post-processing such as assembly, joining, etc., reduction in energy consumption and manufacturing costs, enabling weight reduction, enhancing productivity while simplifying the production of complex parts, and lowering carbon dioxide emissions [13,14]. The culmination of these described advantages and the inherent localization of the PBF process could make it particularly well-suited for the production of new MMC materials for high-temperature applications. Several different studies have been reported to date on the production of boride [15–17], carbide [18–20], nitride [21–23], and oxide [24,25] reinforced MMCs using AM methods. In addition, several studies have been reported recently for superalloy metal matrices with ceramic reinforcements, e.g. In625/WC [26], In625/TiC [27,28], In625/VC [29], In625/TiB_2 [30,31], Hastelloy X/TiB_2 [32], In718/TiC [33], In718/TiC/B_4C [34], In718/WC [35], In718/BN [36].

In the studies mentioned above, the mechanical properties of the superalloy MMCs were enhanced with ceramic reinforcements. Zhang et al. [31] produced TiB_2-reinforced In625 superalloy MMCs by laser-aided additive manufacturing. It was reported that the microhardness, tensile strength, and elongation values were enhanced while the wear rate and coefficient of friction were reduced due to the aggregation of nano-sized TiB_2 in grain boundaries [31]. In another study conducted by Zhang et al. [32], 2 wt% TiB_2 reinforced Hastelloy X crack-free superalloy MMCs were prepared by LPBF. They reported an increase of 43.4 % in hardness, 50.8 % in high-temperature hardness and 28 % in yield strength [32]. Promakhov et al. [37] studied the influence of 5 wt% NiTi–TiB_2 addition to In625 produced by direct laser deposition. It was reported that In625 + 5 wt% NiTi–TiB_2 composite parts produced with direct laser energy deposition achieved increases in microhardness (4.42 GPa vs 2.73 GPa), yield strength (550 MPa vs 545 MPa), and tensile strength (920 MPa vs 850 MPa) compared to pure In625 while maintaining good elongation (33 % vs 48 %) [37]. Zhang et al. [38] also demonstrated the improvements in high-temperature tensile properties that can be achieved with diboride-enhanced nickel superalloys by producing a 2 wt% TiB_2-doped Haynes 230 alloy that showed remarkably higher ductility at 850 °C (~50 % tensile strain) compared to that of undoped Haynes 230 (~10 % tensile strain).

Although there are several different compositions of TiB_2-fortified superalloy MMCs produced with different additive manufacturing methods, the effects of other transition metal diborides as nano-reinforcements are not yet well explored. Many transition metal diborides with melting temperatures higher than 3000 °C, also known as ultra-high temperature ceramics (UHTCs), exhibit superior hardness, oxidation resistance, and chemical inertness at elevated temperatures, making them attractive candidates for the formation of new MMCs [39–42]. In this study, we have selected to analyze the feasibility of ZrB_2 as a reinforcing material, as its relatively lower density and good mechanical properties and corrosion resistance [43] were expected to prove favorable for complementing the properties of the superalloys. To verify this, 2 vol% ZrB_2 nanoparticle-fortified In718 parts have been produced via LPBF. Herein, we describe the microstructural and mechanical characteristics of the ZrB_2 fortified In718 parts evaluated under room temperature and high-temperature conditions in comparison to unfortified In718 parts prepared following the same procedure.

2. Material and methods

2.1. Feedstock preparation

In this study, Inconel 718 (In718) powders were acquired from MSE Supplies LLC, Tuczon, AZ, USA with particle size ranges from 15 to 45 μm. The chemical composition of the as-received In718 powders is provided in Table 1. ZrB_2 powders with particle diameters less than 100 nm were purchased from US Research Nanomaterials Inc. The SEM image (Fig. 1(a)) confirms that the ZrB_2 powders are agglomerated and have particle sizes below 100 nm. These ceramic powders were combined with In718 powders to form a mixture of 2 vol% ZrB_2 and blended in batches of 500 g in a high-speed blender (VM0104, Vita-Mix, USA) for 90 min. The SEM images and EDX mappings of In718+ZrB_2 powders after blending are shown in Fig. 1(d–i). The In718 powders retained their sphericity after mixing with sub-micron ZrB_2 powders. Fig. 1(b–c) shows the zoomed-in SEM micrographs of individual particle surfaces of the as-received In718 and mixed In718+ZrB_2 powders, respectively. The surface texture of commercial In718 (Fig. 1(b)) is quite different than that of the In718+ZrB_2 powder surface (Fig. 1(c)) and shows dendritic grains instead of decorated nanoparticles. EDX results comparing regions Fig. 1(b) and (c) are also presented in Table 1 and confirm that the surface of the In718 particles were effectively decorated with ZrB_2 after high-speed blade mixing.

2.2. LPBF and heat treatment process

As-purchased, unfortified In718 powders and blade-mixed 2 vol% ZrB_2 fortified In718 composite powders were printed via LPBF using a commercial system (EOS M290). The parameter set was determined based on data from previously published LPBF studies of In718 [44–47]. Table 2 shows the printing parameters applied to both In718 and 2 vol% ZrB_2 fortified In718 composite samples (hereon referred to as In718+ZrB_2). Fig. 2(a) displays In718+ZrB_2 before removal from the AISI 4140 Steel build plates. Both room-temperature (RT) and high-temperature tensile specimens and their corresponding dimensions are also shown in Fig. 2(b) and (c), respectively.

Following removal from the build plate by wire electron discharge machining (EDM), samples of both the fortified and unfortified In718 materials were subjected to a standard heat treatment that is applied for wrought In718 in a tube furnace (OTF-1200X) [48], which is described in Table 3 below.

2.3. Materials characterization

Firstly, the samples were cut, ground and polished prior to characterization experiments. The phase composition of LPBF processed samples were characterized by X-ray diffraction (Malvern Panalytical Ltd, Malvern, UK) using Cu Kα ($\lambda = 0.154$ nm) radiation over the range of scattering angles between $2\theta = 10–90°$. To determine the microstructural characteristics and chemical composition, a Zeiss Merlin high-resolution scanning electron microscope (SEM) (Carl Zeiss AG, Oberkochen, Germany) was used. Electron backscatter diffraction (EBSD) analyses were performed in the same SEM. A Zeiss Vision 40 CrossBeam focused ion beam (FIB) was utilized to prepare samples for transmission electron microscopy (TEM). Following FIB, TEM was carried out in a JEOL 2010F field emission STEM (JEOL Ltd., Tokyo, Japan) at 200 kV. UV–vis absorbance values were calculated for pure In718 and In718+ZrB_2 powders using the Universal Reflectance Accessory on a PerkinElmer 1050 UV/VIS/NIR Spectrophotometer. Porosity quantity and distribution for printed samples were analyzed via computed tomography (CT) in a Zeiss Xradia 620 Versa X-ray microscope. Vickers hardness values of the LPBF processed samples were obtained from indentation tests using a Struers/Emco-Test DuraScan Automatic Hardness Tester (Struers LLC, Cleveland, OH, USA) under a load of 0.5 kg (4.903 N) for 10 s. 10 successive indentations were carried out for all

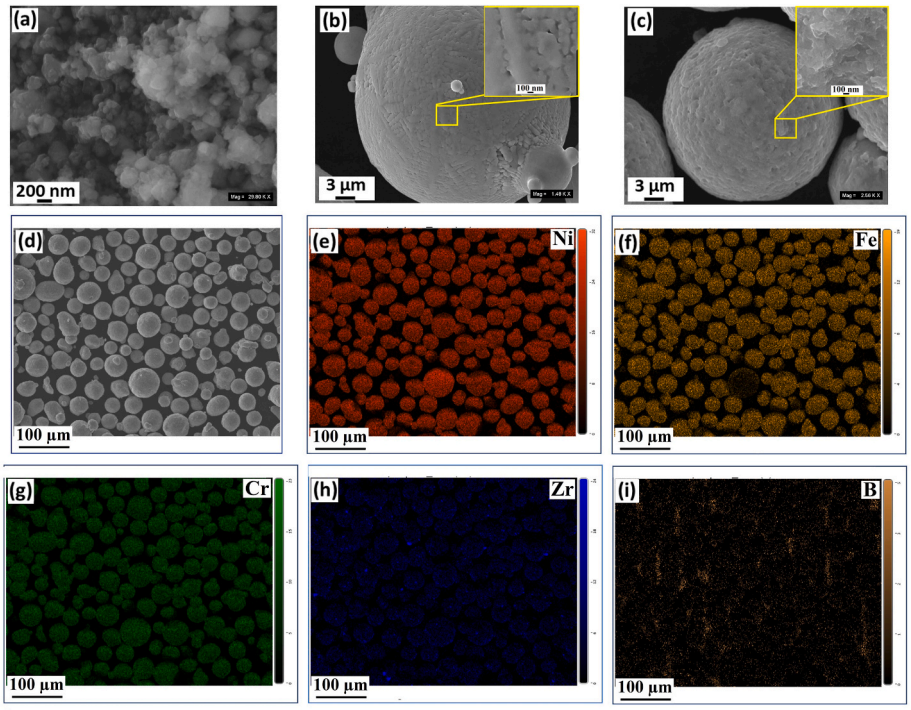

Fig. 1. SEM micrographs of **(a)** commercial ZrB_2 powders, **(b)** In718 particle surface before blending, and **(c)** ZrB_2 decorated In718 particle surface after blending. **(d–i)** SEM micrographs and EDX mappings of In718+ZrB_2 powders after blending.

Table 1
EDX results obtained from as-recieved In718 powders, the surface of In718 particles before blending (Fig. 1(b)), and the surface of In718+ZrB2 particles after blending (Fig. 1(c)).

Element (wt%)	as-recieved In718 powders	Fig. 1(b)	Fig. 1(c)
Ni	52.49	49.88	45.03
Fe	19.97	20.29	18.17
Cr	17.21	21	18.08
Nb	4.75	3.79	3.11
Mo	2.9	3.17	3.19
Ti	0.89	1.1	1.02
Co	0.95	0.11	0.17
V	0.73	0.03	0.01
Mn	0.11	0.03	0.01
Al	–	0.14	0.26
Zr	–	0.44	7.08
B	–	0.02	3.87

Table 2
LPBF process parameters.

Laser process parameter	Value
Laser powder (W)	285
Scanning speed (mm/s)	960
Layer thickness (μm)	40
Hatch spacing (μm)	110
Laser spot size (μm)	100
Scan rotation (∘)	67
Volumetric energy density (J/mm^3)	67.47
Build plate temperature (°C)	80
Shield gas and its purity	Ar, 99.9 %
Build plate material	4140 steel

the samples, and the average Vickers hardness values with their standard deviations are reported. Tensile tests were performed at room temperature in an Instron 5969 with a strain rate of 2×10^{-4} s^{-1} and repeated two times for each sample category to verify results. The tensile displacement and the strain were precisely recorded by a non-contact AVE2 video extensometer. High-temperature tensile tests were performed at 650 and 800 °C with a 2×10^{-4} s^{-1} strain rate using a custom-built tensile tester equipped with a furnace operating up to 1000 °C. The tensile tester consists of a linear actuator (Physik Instrument (PI) GmbH & Co.), load cell (FUTEK Advanced Sensor Technology, Inc.), and an XYZ linear stage. The strain in the gauge section was accurately measured by the digital image correlation (DIC) technique. For stable DIC strain measurement at elevated temperatures, white aluminum oxide aerosol paint and black heat-resistant paint were sprayed on the gauge section of each specimen to create high-contrast speckle patterns. Sample images were captured every 2 s during the test using a CCD camera (Teledyne FLIR, Inc.) with a telecentric lens (Edmund Optics, Inc.).

3. Results and discussion

After fabrication of the In718 and In718+ZrB_2 composites, SEM/EDX analysis was performed on as-printed and heat treated (HT'ed) samples. Low-magnification SEM images seen in Fig. 3(a and c) revealed spherical pores in the microstructures of as-printed and HT'ed In718 samples, which are indicated by white arrows. These are believed to be gas porosities, which might have formed during LPBF. The described pores were not observed in the In718+ZrB_2 composites (Fig. 3(b and d)), which were LPBF'ed under the same conditions optimized for unfortified In718. These findings are consistent with our previous findings for In718+SiC composites [49], which would seem to suggest that the incorporation of ceramic nanofillers may reduce the formation of defects associated with the 3D printing process. It was also noted that the grain size of the In718+ZrB_2 samples were strikingly smaller compared to those of unfortified In718, a phenomenon that is independent of heat treatment. The difference in grain shapes and sizes between unfortified and ZrB_2-fortified In718 samples will be further discussed under EBSD findings later. High magnification SEM images also revealed Laves phases formed in the In718+ZrB_2 matrix, indicated by blue arrows (Fig. 3(f and h)) with their corresponding elemental distributions listed in Table 4 (EDX point 1 and 3). High wt% concentrations of Nb and Mo

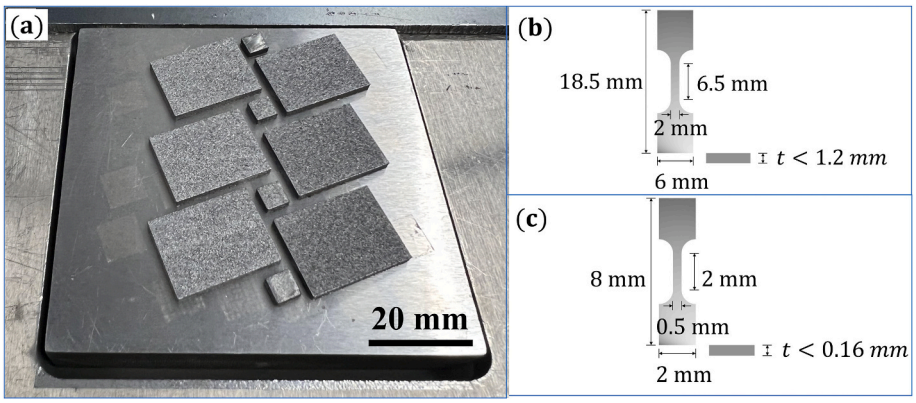

Fig. 2. (a) In718+ZrB_2 samples fabricated in EOS M290 SLM printer, **(b)** Geometry and dimensions of RT tensile specimen machined by wire EDM, and **(c)** Geometry and dimensions of high-temperature tensile specimen machined by wire EDM.

Table 3
Heat treatment performed on LPBF'ed samples.

Heat Treatment Steps	Heat Treatment Conditions
Step 1	1050 °C/15 min, water cooling
Step 2	720 °C/8 h, furnace cooling
Step 3	620 °C/8 h, air cooling

confirmed the existence of Laves phases in the microstructure. Additionally, fine dark spots (notated by red arrows) with diameters less than 100 nm were scattered over the matrix of as-printed and HT'ed In718+ZrB_2 samples. EDX analysis obtained from points 2 and 4 showed that these dark spots were enriched with Ni and Zr but lacking B. This observation suggests a possible decomposition of ZrB_2 during LPBF. EDX mapping results obtained from as-printed In718+ZrB_2 also clearly confirmed the presence of small Zr-rich particles distributed throughout the In718 matrix and also Nb,Mo-rich Laves phases (Fig. 3(i–p)).

In order to perform a more in-depth analysis of the porosity formation during printing, we performed X-ray CT analysis on samples of as-printed In718 and In718+ZrB_2, as shown in Fig. 4. Results were taken from central regions more than 150 μm from each sample face to avoid edge effects of printing or EDM. Utilizing the previously described laser parameters based on literature optimization of unfortified In718, CT results indicated that the In718 sample achieved 99.90 % density, with 95 % of pores having a maximum Feret diameter <90 μm and the largest pore having a diameter of approximately 180 μm. On the other hand, the addition of 2 vol% ZrB_2 was found to increase density to >99.99 % and decrease pore size such that 95 % of pores had maximum Feret diameters <40 μm and maximum pore diameter was found to be less than 50 μm, confirming the improvement in print quality observed under SEM. This data is provided in a histogram in Fig. 4(c).

Such a decrease in as-printed porosity is a major boon of the present reinforcement process, even when considered separately from improvements in mechanical properties discussed later in this paper. Low

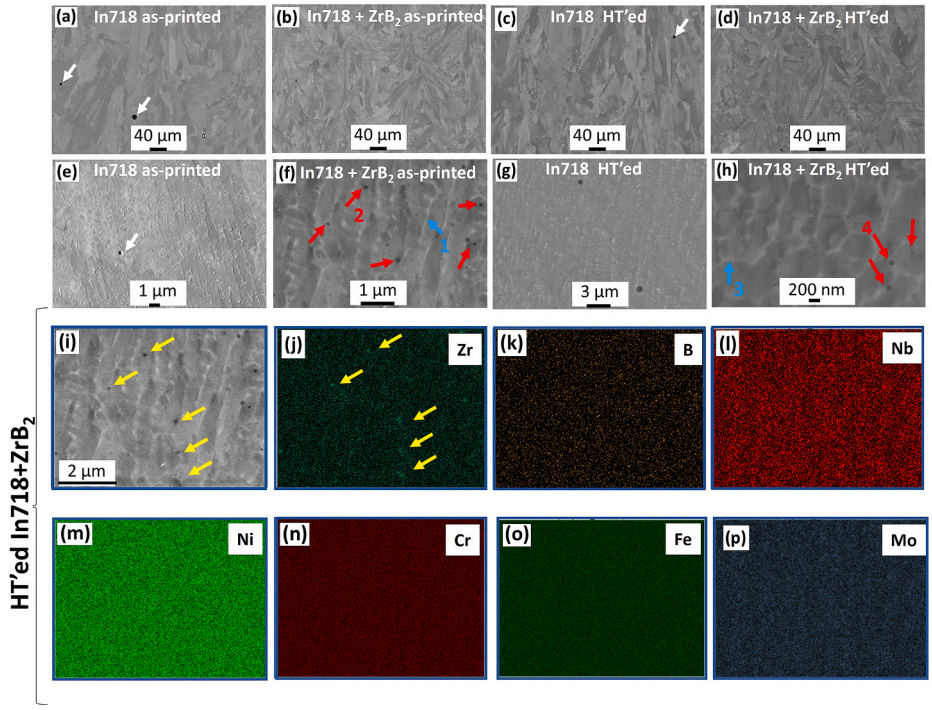

Fig. 3. (a–h) Secondary electron SEM images obtained from LPBF'ed samples (white arrows indicate pores, blue arrows indicate Mn–Mo rich regions, red arrows indicate Zr-rich regions), and **(i–p)** EDX mapping analysis obtained from HT'ed In718+ZrB_2 (yellow arrows indicate Zr-rich regions). (For interpretation of the references to colour in this figure legend, the reader is referred to the Web version of this article.)

Table 4
EDX Analysis of points 1–4 from Fig. 3.

Element (wt%)	Point 1	Point 2	Point 3	Point 4	General EDS obtained from as-printed In718+ZrB_2
Ni	53.85	37.35	52.37	37.63	51.68
Fe	15.12	9.76	17.23	8.98	18.15
Cr	10.82	1.90	10.75	1.12	18.44
Nb	10.39	–	10.13	–	4.58
Ti	0.93	–	0.72	–	0.7
Al	0.7	–	0.48	–	0.89
Mn	0.05	–	0.13	–	0.08
Si	0.36	–	0.35	–	0.37
Mo	7.51	–	7.55	–	2.73
Zr	0.19	50.88	0.21	52.11	1.84
B	0.08	0.11	0.08	0.16	0.54

relative density compared to traditional casting methods remains a downfall of AM processes that may impede more widespread adoption. Lowering pore number density and size are essential to decreasing the likelihood of crack formation and propagation under stress and fatigue, which are especially tied to the size and geometry of the largest pores. The results presented in Fig. 4 are therefore considered to be a significant success of the In718+ZrB_2 MMC, and understanding the key mechanisms of this improvement will likely prove valuable to future material design. One theory considered to explain the significant decrease in as-printed porosity with ceramic reinforcement was that the formation of a ceramic coating on the surface of the metal particles decreases laser reflection off the particle surfaces, thereby increasing energy absorption for more uniform melting. To test the plausibility of this theory, UV–vis measurements were carried out on the powders in a spectrophotometer using a Universal Reflectance Accessory. At relevant wavelengths (1060–1100 nm), In718+ZrB_2 was found to have a slightly higher absorbance than unfortified In718 (approximately 52.5 % vs 51.9 %) as predicted, but we do not expect that this slight increase sufficiently explains the difference between 99.90 % density and 99.99 %. The absorbance of the liquid after melting might be expected to play a larger role, but this in-situ measurement was outside the realm of capabilities for the present experimental setup in a commercial printer and is recommended for future studies. Another suggestion is that the addition of ceramic particles may have increased the viscosity of the melt pool and decreased spattering during laser melting, resulting in fewer unmelted particles that could have disrupted the solidification process. Such a result has been recently reported for TiC nanoparticles in Al6061 by Qu et al. [50].

XRD and STEM/EDX analyses were carried out to reveal the final phase distributions in the HT'ed In718+ZrB_2 samples. XRD analysis in Fig. 5(a) showed only the typical face-centered cubic γ (Ni–Cr–Fe) matrix phase. It was concluded that the XRD peaks of potential secondary phases (i.e. Zr-rich phase seen in SEM/EDX analysis) were not observed after LPBF or HT, most likely due to the relatively low volume fraction of ZrB_2 (2 vol%) in the starting composite powder batch. However, STEM/EDX analysis shed light on the phase transformations which took place in HT'ed In718+ZrB_2. The first STEM/EDX mapping provided in Fig. 5 (b–h) below shows regions enriched with Ni, Ti, Nb, Al and depleted of Fe and Cr. This reveals the formation of Ni–Ti–Nb–Al rich precipitates, which are the typical γ′ and γ″ phases that formed during HT in In718+ZrB_2. The region surrounded by a white dashed line in Fig. 5 (b–h) is an exemplary location where the precipitates can be observed. On the other hand, the second STEM/EDX mapping provided in Fig. 5 (i–p) reveals the decomposition of ZrB_2 into Zr and B. Based on these results, it seems clear that the decomposition of ZrB_2 during LPBF was followed by a series of chemical reactions between several elements (i.e., Ni, Zr, B, Nb, Mo, Cr) forming intermetallic compounds and complex borides. It is important to note that similar phase transformations were observed in the as-printed In718+ZrB_2 sample, which is shown by SEM/EDX analysis in Fig. S1 of the Supplementary Materials. The regions notated by yellow arrows clearly indicate the formation of (Zr,Ni)-based intermetallic nanoparticles (below 200 nm), whereas the regions indicated by red arrows show the existence of (Nb, Mo, Cr)-rich boride nanoparticles (between 100 and 200 nm). It could be stated that the free B diffused into boride-forming elements (Nb, Mo, Cr) to form complex

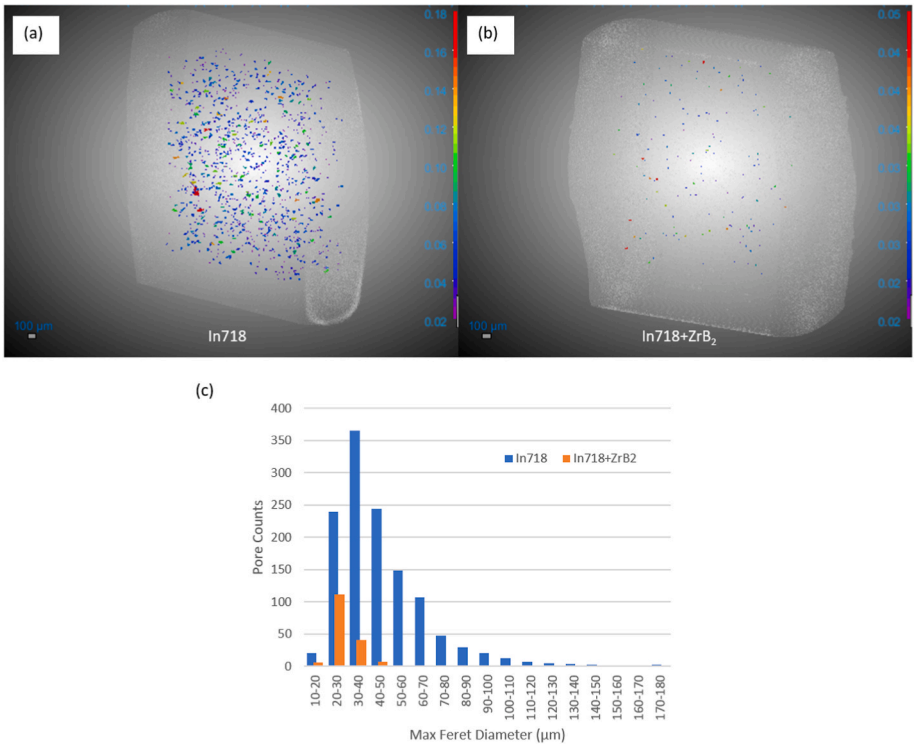

Fig. 4. X-ray CT reconstructions displaying pores with diameters >20 μm formed during printing of **(a)** In718 and **(b)** In718+ZrB_2 samples. **(c)** Histogram of pore counts for unfortified and fortified samples organized by maximum Feret diameter.

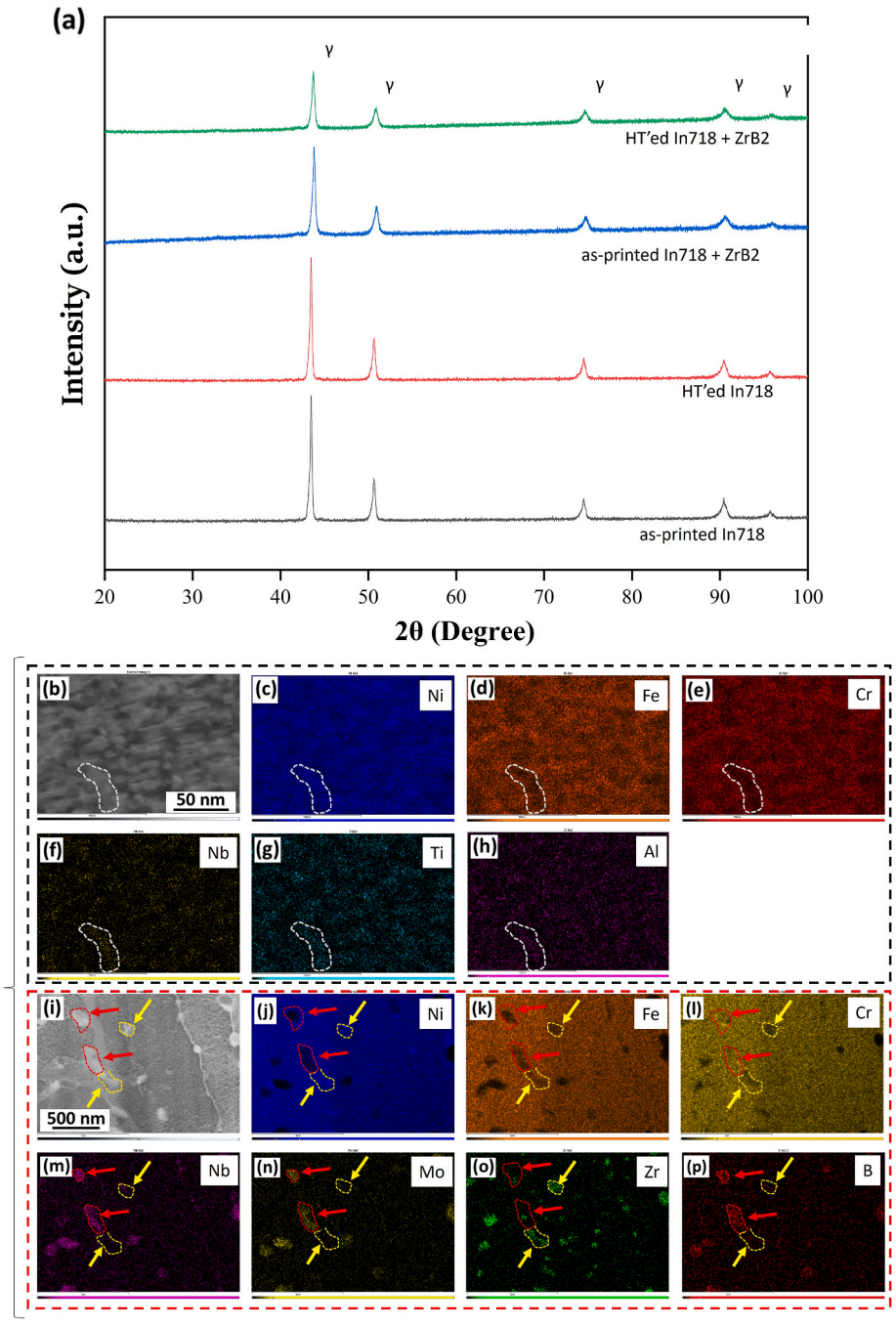

Fig. 5. STEM/EDX mapping analysis obtained from HT'ed In718+ZrB_2 showing: **(a–g)** γ' and γ'' precipitates (white dashed regions) and **(h–o)** (Nb, Mo, Cr)-based borides and (Zr,Ni)-based intermetallic nanoparticles (red arrows indicate Nb,Mo,Cr,B-rich regions, yellow arrows indicate Zr, Ni-rich regions). (For interpretation of the references to colour in this figure legend, the reader is referred to the Web version of this article.)

borides, while the free Zr reacted with neighboring Ni elements during LPBF to form (Zr,Ni)-based intermetallics. It is also noted that the (Zr, Ni)-based intermetallics are well-known for their thermal and mechanical stability and this makes them a great dispersion-strengthening constituent in alloy systems [51]. This was confirmed after comparing the high-temperature tensile properties of pure In718 and In718+ZrB_2, which will be discussed later.

Fig. 6 displays a STEM/EDX mapping analysis focusing on an exchange reaction zone between Zr, B, Nb, Mo and Cr in HT'ed In718+ZrB_2. Three different phase zones are observable in Fig. 6(a), and the corresponding EDX results of the related phase regions are also listed in Table 5. The region surrounded by the purple line was found to be rich in Nb, Mo, Cr and B elements, indicating the formation of (Nb,Mo,Cr)-based complex borides. Meanwhile, another phase region (surrounded by the blue line) was observed adjacent to the (Nb,Mo,Cr)-based boride region and showed high Zr and Ni signals. This supports that the (Nb, Mo,Cr)-based boride formation was promoted by free B released by the decomposition of ZrB_2 nanoparticles during LPBF. STEM/EDX line scan analysis also confirmed the composition of these precipitates (Fig. 6(b)). Subsequently, selected area electron diffraction (SAED) patterns and high-resolution TEM (HR-TEM) images were acquired to evaluate the coherence of these precipitates with the surrounding matrix. SAED analysis, presented in Fig. 6(c), revealed a crystalline structure closely resembling that of the matrix. Moreover, through HR TEM imaging of

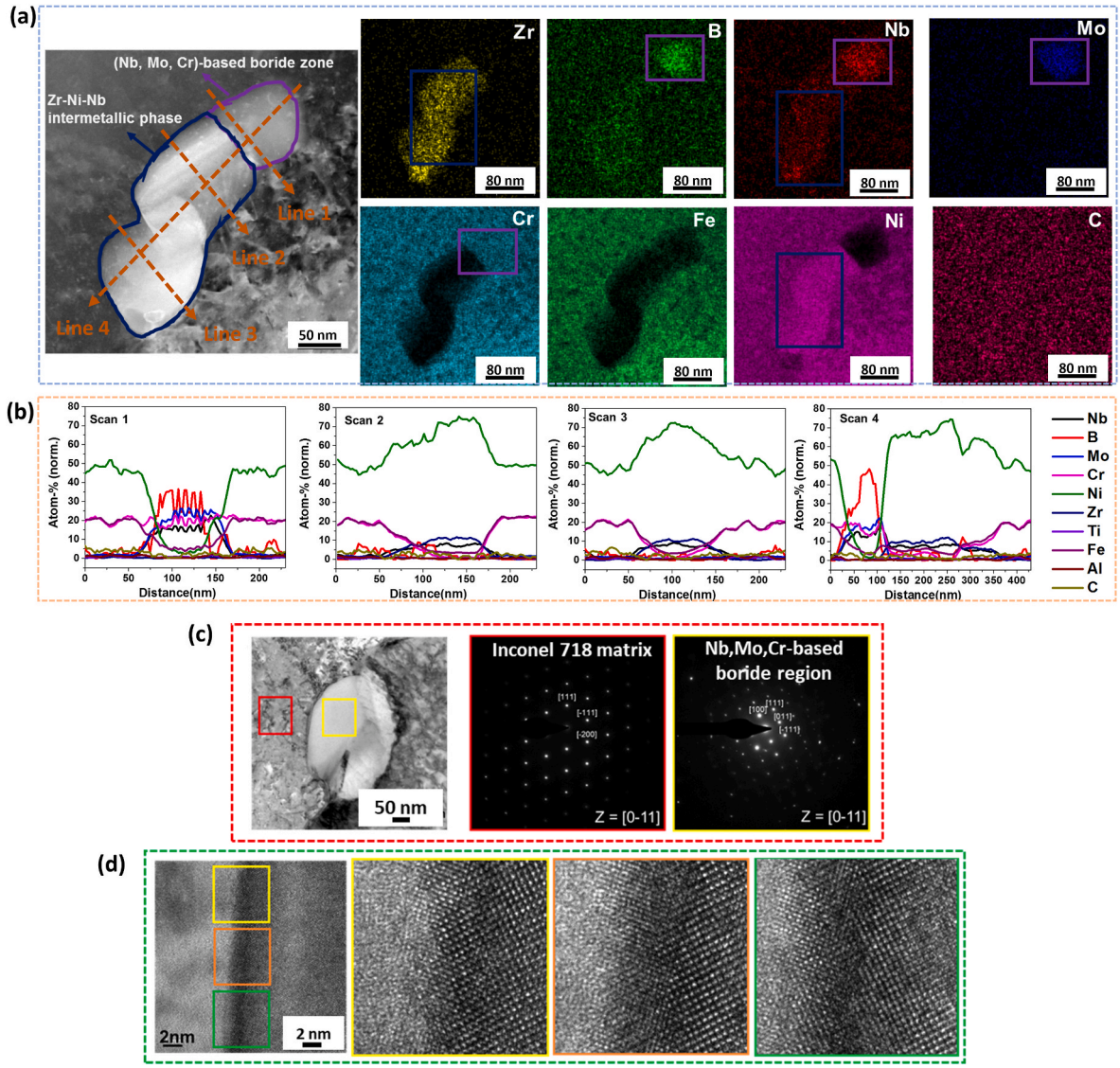

Fig. 6. (a) High magnification STEM/EDX mapping analysis obtained from HT'ed In718+ZrB_2 focusing on an exchange reaction zone between Zr, B and Nb, Mo, Cr, **(b)** High magnification STEM/EDX line profiles obtained from HT'ed In718+ZrB_2 focusing on exchange reaction zone between Zr, B and Nb, Mo, Cr (The EDX lines are shown as orange dashed lines in Fig. 6(a)), **(c)** SAED patterns obtained from matrix and boride-rich regions of HT'ed In718+ZrB_2 and **(d)** HR-TEM images obtained from the matrix and boride-rich interface of HT'ed In718+ZrB_2. (For interpretation of the references to colour in this figure legend, the reader is referred to the Web version of this article.)

Table 5
EDX analysis obtained from different phase zones shown in Fig. 6.

Element (wt%)	(Nb,Mo,Cr)-based boride zone	Zr–Ni intermetallic zone
Ni	–	46.18
Fe	–	1.26
Cr	20.60	1.49
Nb	27.54	–
Mo	22.83	–
Zr	–	51.07
B	29.03	–

the interface between the matrix and the boride phase, we confirmed the presence of well-bonded phase boundaries, as visually demonstrated in Fig. 6(d).

Next, EBSD was performed on In718 and In718+ZrB_2 samples with and without HT. Fig. 7(a–d) shows the EBSD orientation maps of each sample and reveals significant grain size reduction, especially in as-printed In718+ZrB_2. Please note that the grain sizes seen in the plots are the maximum feret diameters measured from individual grains. The calculated average grain sizes of as-printed In718, as-printed In718+ZrB_2, HT'ed In718 and HT'ed In718+ZrB_2 were 136.3, 31.1, 78.8 and 47.9 μm, respectively. As-printed In718 was observed with grain sizes up to almost 400 μm, whereas the maximum grain size of the as-printed In718+ZrB_2 was below 100 μm (Fig. 7(e)). After HT, the maximum grain size of the unfortified In718 decreased considerably to less than 240 μm, but this value was still almost twice the maximum grain size of HT'ed In718+ZrB_2. It is well known that the incorporation of fine ceramic borides could hinder the grain growth of alloys during solidification if they are homogeneously distributed in liquid metal [52, 53]. Therefore, this finding confirms that ZrB_2 also has a high potential for producing fine-grained nickel-based metal matrix composites via LPBF. Another striking result was the remarkable difference in grain misorientation distributions between unfortified and ZrB_2 fortified samples after LPBF (Fig. 7(f)). It was quite clear that the fraction of the low-angle grain boundaries was lower in the as-printed In718+ZrB_2 samples compared to the as-printed In718, although the grain misorientation angle distributions became closer after heat treatment. It could

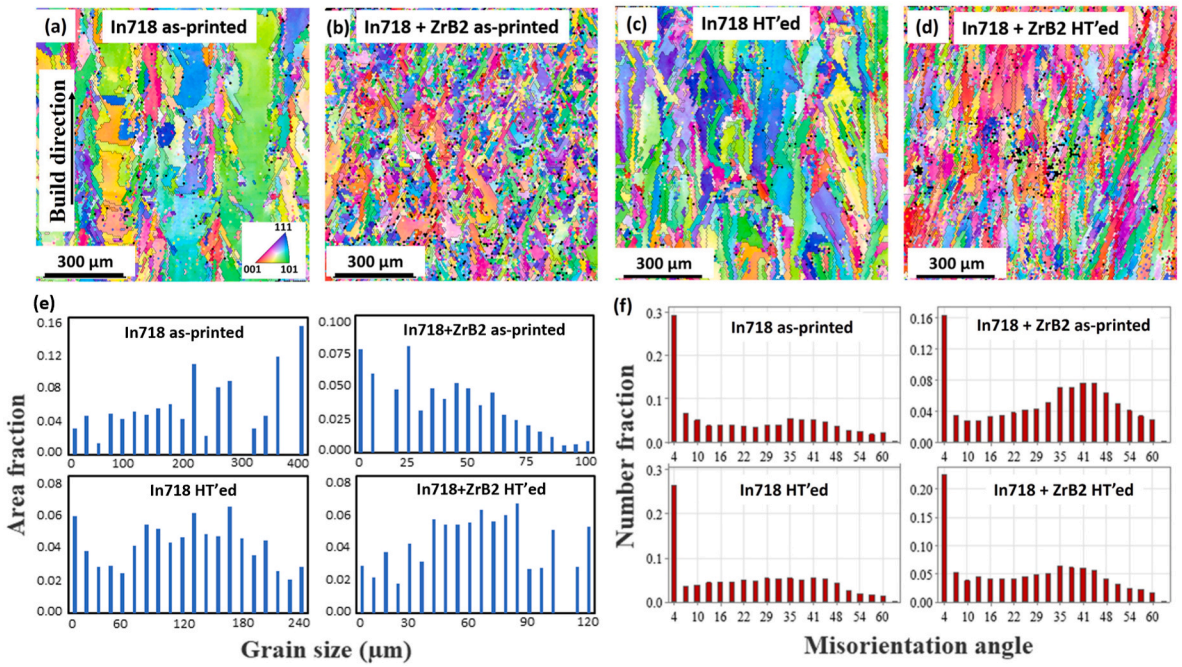

Fig. 7. (a–d) EBSD orientation maps obtained from LPBF'ed samples and corresponding **(e)** grain size distribution and **(f)** misorientation angle distribution plots.

be stated that the thermal stresses experienced during LPBF of In718 caused a greater fraction of high dislocation density regions and facilitated the formation of low-angle grain boundaries [54,55]. This is also promising because it suggests that the addition of ZrB_2 reduces thermal stress accumulation during LPBF, which has significant potential to enable the production of crack-free complex geometries via LPBF.

After characterizing the microstructural features, mechanical tests were carried out. Microhardness results for the as-printed and HT'ed In718+ZrB_2 were 476 and 576 HV, respectively (Table 6). This corresponds to an increase of 49 % in the as-printed and 32 % in the HT'ed state by dispersing ZrB_2 into In718. The microhardness values are also remarkably higher than those of In718+SiC composites that were LPBF'ed and HT'ed in our previous study [49]. The finding is consistent with previous research by Zheng et al. [52], who reported that the microhardness of LPBF'ed In718 (as-printed condition) increased by nearly 100 % upon adding 5 vol% TiB_2 into In718. Considering that the volumetric fraction of ZrB_2 in our study is less than half of that in the aforementioned study, the 49 % increase in hardness after ZrB_2 incorporation seems strikingly effective as well. It appears that the formation and homogeneous distributions of (Zr,Ni)-based intermetallic and (Nb, Mo, Cr)-based boride nanoparticles in the matrix, lower porosity, and finer grain size distribution of In718+ZrB_2 resulted in exceptional microhardness values compared to pure In718.

Room temperature tensile stress-strain curves of pure In718 and In718+ZrB_2 are shown in Fig. 8(a). The as-printed In718+ZrB_2 showed significantly higher RT yield strength (σ_{YS}) and ultimate tensile strength (σ_{UTS}) compared to the as-printed pure In718. However, the RT elongation was below 10 %, a significant decrease compared to the as-printed In718 (around 30 %). The RT σ_{YS} and RT σ_{UTS} of HT'ed In718+ZrB_2 increased by 13 % and 15 %, respectively, compared to its as-printed counterpart. The RT elongation of the HT'ed ZrB_2 decreased to 5 %, which is still acceptable for many applications. Fig. 8(b) provides a table that lists sample number identifiers for several LPBF'ed In718 composite compositions with and without heat treatment [48,49,56,57]. The RT mechanical properties of these samples are compared in Fig. 8(c) and (d). The LPBF'ed In718+ZrB_2 samples in this study exhibited remarkably higher strength but relatively lower elongation compared to similar LPBF'ed composite samples, irrespective of the heat treatment. The improvements in RT σ_{YS} and RT σ_{UTS} of In718+ZrB_2 samples suggest that the (Zr,Ni)-based intermetallic and (Nb,Mo, Cr)-based boride nanoparticles play a critical role in the strengthening effects, resulting from interactions with dislocations, as well as their effects on the grain size distribution and lower porosity.

The high-temperature mechanical behavior of the HT'ed In718 and In718+ZrB_2 was tested at 650 and 800 °C. Despite the widely recognized upper-temperature limit for long-term structural usage of In718 being 650 °C [58], high-temperature tensile tests were conducted up to 800 °C to gain an understanding of the mechanical behavior of the In718+ZrB_2 system in harsher environments. As presented in Fig. 9 and Table 7, In718+ZrB_2 achieved $\sigma_{YS} = 1008$ MPa and $\sigma_{UTS} = 1162$ MPa, which are approximately 15 % higher than pure In718 at 650 °C. However, the addition of ZrB_2 to In718 resulted in a slight decrease in elongation at 650 °C, indicating that the enhancement in strength (10–15 %) came with a cost of a decrease in ductility at 650 °C. The low elongation of In718 at 650 °C is not surprising [59,60]. Sun et al. [60] demonstrated that the elongation of printed In718 alloy could be as low as 1 %, depending on the built direction. In another study, Sang et al. [58] reported that the elongation of In718 is 2–3% at 650–750 °C. Surprisingly, the elongation of the HT'ed In718+ZrB_2 at 800 °C increased considerably to almost 10 %. This is remarkable given that pure In718 exhibited a further decrease in ductility when the temperature increased from 650 °C to 800 °C, while In718+ZrB_2 showed the opposite trend. This behavior is a complete reversal of the trend established from RT and 650 °C tensile tests, where the inclusion of ZrB_2 resulted in the loss of ductility. Zhang et al. [38] also reported a similar behavior in TiB_2--fortified Haynes 230 alloy. They showed that 2 wt% TiB_2 fortified Haynes 230 alloy showed exceptional ductility at 800 °C (~50 % tensile

Table 6
The average microhardness of as-printed In718, HT'ed In718, as-printed In718+SiC, and HT'ed In718+SiC samples.

Material	Microhardness value (HV)
In718 as-printed [49]	319.1 ± 7.9
In718 HT'ed [49]	436.3 ± 11.3
In718+SiC as-printed [49]	363 ± 10.2
In718+SiC HT'ed [49]	468.9 ± 8.7
In718+ZrB_2 as-printed (this study)	475.7 ± 13.0
In718+ZrB_2 HT'ed (this study)	576.2 ± 10.6

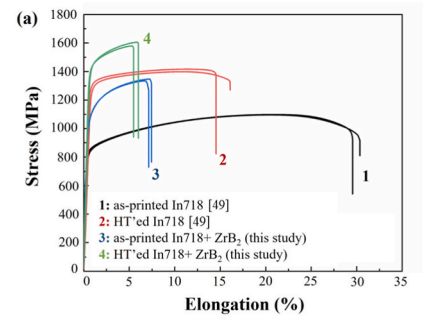

(b)

Sample	Material	Ref
1	as-printed In718	[49]
2	HT'ed In718	[49]
3	as-printed In718+ZrB_2	(this study)
4	HT'ed In718+ZrB_2	(this study)
5	as-printed In718+SiC	[49]
6	HT'ed In718+SiC	[49]
7	as-printed In718+2 wt%TiC	[56]
8	HT'ed In718+2 wt%TiC	[56]
9	as-printed In718+1 wt%Y_2O_3	[57]
10	AMS 5662G specification for wrought In718	[48]

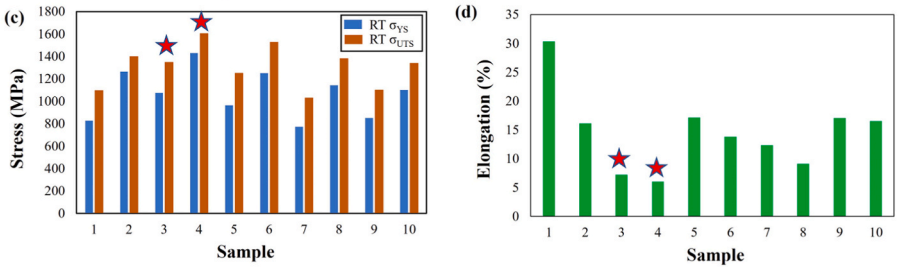

Fig. 8. (a) Room temperature tensile stress-strain curves of pure In718 [49] and In718+ZrB_2, **(b)** Table listing the sample number vs materials, **(c)** Comparison of room temperature σ_{YS} and σ_{UTS} of several LPBF'ed In718 and In718-based composites with and without heat treatment, and **(d)** Comparison of room temperature elongation (%) of several LPBF'ed In718 and In718-based composites with and without heat treatment.

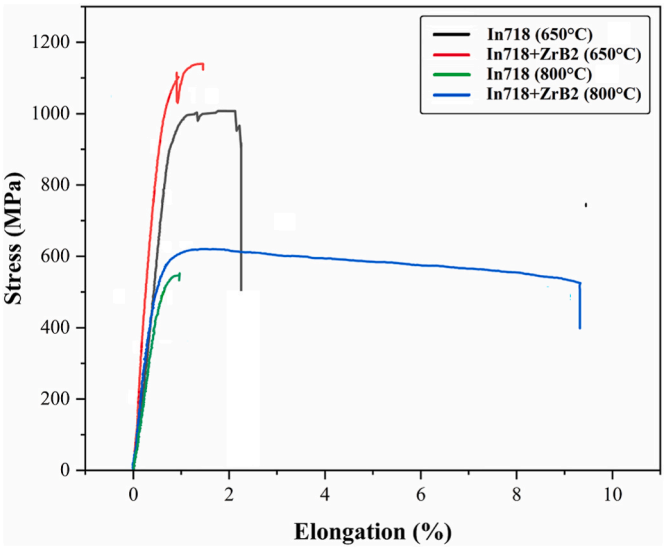

Fig. 9. High-temperature tensile stress-strain curves for HT'ed In718 and In718+ZrB_2 samples.

Table 7
High-temperature tensile test results obtained from HT'ed In718 and In718+ZrB_2 samples.

Sample	HT'ed In718	HT'ed In718+ZrB_2
650 °C σ_{YS} (MPa)	983.4	1086.7
650 °C σ_{UTS} (MPa)	1008.0	1162.3
650 °C Elongation (%)	2.1	1.5
800 °C σ_{YS} (MPa)	501.3	552.2
800 °C σ_{UTS} (MPa)	556.2	603.1
800 °C Elongation (%)	1.0	9.2

strain) compared to that of unfortified Haynes 230 (~10 % tensile strain). Low ductility accompanied by a sharp drop in strength is within expectations for In718 since this temperature regime is far above the traditional In718 operation temperature limit. However, HT'ed In718+ZrB_2 seemed to retain and even expand its ductility at extreme temperatures. Furthermore, the σ_{YS} and σ_{UTS} In718+ZrB_2 were also higher (10 % and 8 %, respectively) than pure In718 at 800 °C. This demonstrates that a significant improvement in toughness and ductility can be attained without compromising the tensile strength.

At high temperatures, the plastic flow of materials can have significant strain-rate sensitivity, $m \equiv d\ln\sigma/d\ln\dot{\varepsilon}$. Higher m can delay the onset of flow localization and alter the trajectory of damage evolution. E. W. Hart showed that the Considère criterion for plastic flow stability $d\sigma/d\varepsilon > \sigma$ needs to be modified to account for the strain-rate sensitivity effect: $d\ln\sigma/d\varepsilon + m > 1$, thus higher m would delay the onset of the plastic flow localization [61]. However, Hart only performed linear instability analysis (localization amplitude is infinitesimal) and did not track the time evolution of the nonlinear instability progression when the localization amplitude is big, which is necessary to track damage evolution. Hutchinson and Neale analyzed the necking instability of materials under uniaxial tension in the nonlinear regime and showed that m can have a much larger numerical effect than the Hart criterion [62] for large-amplitude strain localization.

While both In718 and In718+ZrB_2, at 800 °C, should have larger m than at RT and 650 °C, due to the restricted length scales in In718+ZrB_2 the impact of m on stabilizing nonlinear necking and damage evolution may well be more prominent in In718+ZrB_2 than in In718 [63], which could be one explanation for In718+ZrB_2 becoming much more ductile than in In718 at 800 °C, but not at 650 °C. In contrast to pure In718, the In718+ZrB_2 composite exhibits a distinctive microstructure featuring not only γ' and γ″ phases but also additional compound phases stemming from the incorporation of ZrB_2. These additional compound phases result in a higher number density of obstacles, impeding the mobility of dislocations within the material. Another study on the mechanical behavior of PH 13-8 Mo maraging steel at elevated temperatures conducted by Z. Huang et al. revealed a further amplification in strain rate sensitivity m at increased temperatures. This phenomenon was attributed to an increased concentration of precipitates [64]. This also yielded an associated enhancement in ductility. In a separate study, Misra et al. proposed deformation twinning as the governing mechanism underlying the heightened strain rate sensitivity m observed in the material [65], where twin boundaries acted as barriers, restricting dislocation motion and impeding dislocation climb.

TEM analysis conducted on the In718+ZrB_2 specimen fractured at

800 °C demonstrated the interactions between compound phases and dislocations within the material (Fig. 10(a)). Specifically, it revealed the presence of entangled dislocation regions proximate to the scattered intermetallic phases, as well as dislocation loops forming around precipitates. In addition to the interactions between intermetallic phases and dislocations, an additional factor contributing to the remarkable ductility exhibited by In718+ZrB_2 at 800 °C may be the formation of serrated grain boundaries (GBs) induced by boron. P. Kontis et al. [66] reported that the incorporation of B into nickel-based superalloys can significantly enhance its ductility, particularly at elevated temperatures such as 750 °C, and at low strain rates, such as 2×10^{-5} s^{-1}. Such segregation serves to facilitate the motion of these boundaries ("lubrication") [67,68], resulting in the formation of serrated GBs [66]. Notably, the presence of serrated GBs significantly contributes to the enhancement of ductility by delaying crack propagation, impeding cavity linkage, and lengthening the path along which cracks propagate along the GBs [66]. Building upon previous research, we investigated the GB characteristics of In718 and In718+ZrB_2 through electron backscatter diffraction (EBSD) analysis. As shown in Fig. 10(b), our analysis revealed a notably enhanced prevalence of serrated GBs in In718+ZrB_2 when compared to In718. Although the strain rate applied in our tensile tests, 2×10^{-4} s^{-1}, was relatively faster than in the reference, it can still be considered relatively slow given that the experiment was conducted at a higher temperature of 800 °C. In particular, under conditions characterized by low strain rates and elevated temperatures, diffusional phenomena at the grain boundaries become prominent. Therefore, it is reasonable to infer that the serrated GB motions in In718+ZrB_2 contribute to the increase in ductility in a manner consistent with prior research finding.

Fig. 11 shows the SEM images taken from the fractured surfaces of HT'ed In718 and In718+ZrB_2. Fracture surfaces of HT'ed In718 and In718+ZrB_2 tested at RT show dimples and porosities (annotated by red arrows), indicating ductile fracture (Fig. 11(a,d)). At 650 °C, the fracture surfaces of both samples displayed brittle fracture morphology, which is consistent with the low measured elongation values of 1–2%. The fracture surface of the HT'ed In718 at 800 °C exhibited sharp and distinct cleavage planes, indicating that brittle fracture had also occurred. However, dimples were also observed on its fracture surface indicating some degree of plastic deformation (as indicated by yellow arrows in Fig. 11(c)). On the hand, the size of dimples on In718+ZrB_2 fracture surface at 800 °C are larger compared to those of pure In718 at the same temperature (as indicated by yellow arrows in Fig. 11(f)). At 800 °C, the fracture surface of HT'ed In718 shows overlapping Nb and Mo signals ((Fig. 11(g)). However, the Nb and Mo rich regions lacks Cr signals as opposed to the SEM/EDX mapping result of the HT'ed In718+ZrB_2 at 800 °C. It could be assumed that Nb and Mo formed intermetallics in the pure In718 whereas Cr and B reacted with Nb, Mo, leading to (Nb,Mo, Cr)-based boride formation in HT'ed In718+ZrB_2. Furthermore, fracture surface of HT'ed In718+ZrB_2 at 800 °C still shows (Zr,Ni)-based intermetallics and (Nb,Mo,Cr)-based boride nanoparticles (Fig. 11(h)). Additional SEM and EDX mapping characterizations can be found in Figs. S2 and S3 of the Supplementary Materials.

4. Conclusions

A ZrB_2-fortified In718-based metal matrix composite was successfully fabricated via LPBF technique. Electron microscopy revealed the dissolution of ZrB_2. This decomposition resulted in the formation of (Zr, Ni)-based intermetallics and (Nb, Mo, Cr)-based boride nanoparticles, which were homogeneously distributed within the In718 matrix. It is concluded that the formation of nanoparticles hampered grain growth during solidification. As a result, In718+ZrB_2 composites possessed significantly smaller grain size than the pure In718 after LPBF. In parallel, X-ray CT of ZrB_2 fortified composites showed both an increase in the as-printed density and a decrease in pore diameters compared to the as-printed In718.

As a result of the microstructural changes, both room-temperature and high-temperature mechanical properties of In718+ZrB_2 MMC were found to be exceptional compared to pure In718. The enhancement in strength of ZrB_2 fortified composites was due to a combination of strengthening mechanisms, including grain size refinement and dispersion strengthening. Specifically, the HT'ed In718 fortified by ZrB_2 showed a 15 % increase in σ_{YS} and σ_{UTS}, though with a significant loss in ductility (5 % tensile elongation) compared to the unfortified In718.

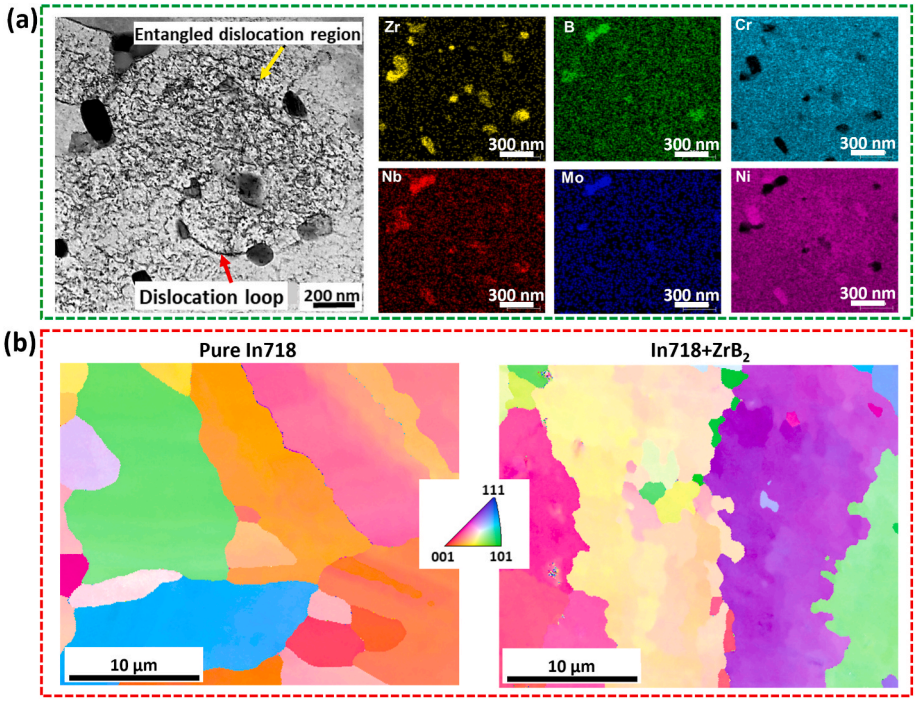

Fig. 10. (a) STEM image and EDX mapping obtained from HT'ed In718+ZrB_2 after 800 °C tensile test showing dislocation loop and entanglement in the microstructure and **(b)** EBSD maps obtained from HT'ed In718 and In718+ZrB_2 showing the difference of grain boundary morphologies.

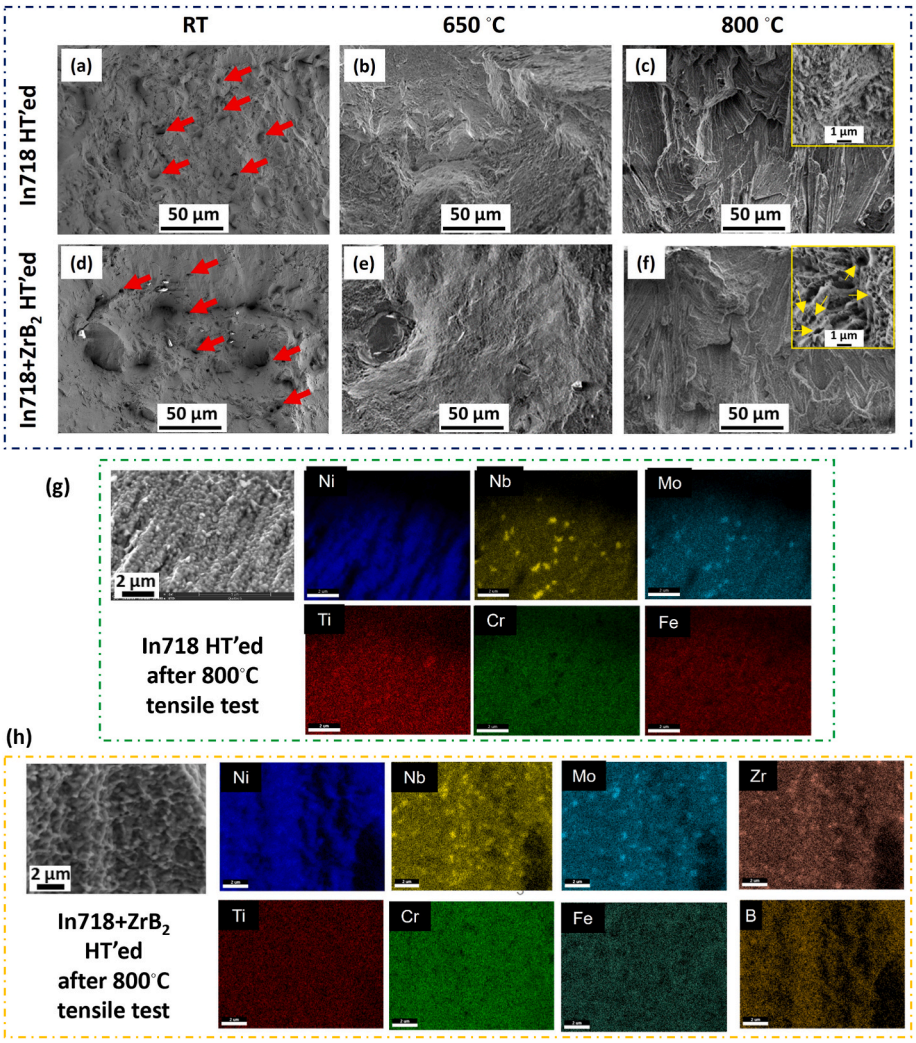

Fig. 11. Fracture surface analysis for tensile tests conducted at different temperatures: **(a–c)** HT'ed In718 and **(d–f)** HT'ed In718+ZrB_2, and SEM/EDX mapping analysis obtained from fracture surfaces of **(g)** HT'ed In718 and **(h)** In718+ZrB_2 after 800 °C tensile test.

High-temperature tensile results were found to be more remarkable. At 650 °C tensile testing temperature, In718+ZrB_2 achieved 10–15 % higher strength than pure In718 with a slightly lower elongation. Moreover, the ZrB_2 fortified composite exhibited a significant increase in ductility at 800 °C, achieving almost 10 % elongation while maintaining higher strength compared to pure In718. These results suggest that the formation of a metal matrix composite doped with ZrB_2 may significantly increase the high-temperature survivability of In718 and potentially raise the upper operating temperature limit in systems where In718 components are currently employed. Thus, the authors believe that the scalable production method for In718+ZrB_2 composites shown in this study holds great potential for manufacturing components to be used in extreme environments such as nuclear fusion reactors and gas turbines.

Author contributions statement

E.T. and A.D.O. and J.S.B. analyzed the results, characterized the materials, and wrote; K.H.L performed HT tensile tests and fracture surface analysis; J. Liu printed samples and performed heat treatment and RT tensile tests; S.K. and D. A. prepared composite powders; Y.Z. collected TEM data; S.Y.K. carried out TEM sample preparation; A.J.H. oversaw the study and provided editing; W.C. oversaw the study and provided editing, G.D.S. and J. Li conceived the project idea, oversaw the study and provided editing.

Declaration of competing interest

The authors declare no competing interests.

Data availability

Data will be made available on request.

Acknowledgment

This work was supported by Eni S.p.A. through the MIT Energy Initiative, The Scientific and Technological Research Council of Turkey (TUBITAK) under Grant No. 1059B192000941, and ARPA-E (DE-AR0001434). Furthermore, 3D printing for this project was completed using the EOS M290 at the Advanced Digital Design and Fabrication core facility at the University of Massachusetts, Amherst. WC acknowledges support by the National Science Foundation (DMR-2004429). ADO acknowledges support by NSF GRFP Award #4999143677. SK and DA acknowledge the support by Istanbul Technical University Scientific Research Projects Unit with a project (No: MUA-2021–43196) entitled "Production and Characterization of Boron Containing Metallic Nanocomposites via Additive Manufacturing". GDS acknowledges support by

the KAI-NEET and UP, KAIST, Korea.

Appendix A. Supplementary data

Supplementary data to this article can be found online at https://doi.org/10.1016/j.compositesb.2023.111052.

References

[1] Lu Y, Wu S, Gan Y, Huang T, Yang C, Junjie L, et al. Study on the microstructure, mechanical property and residual stress of SLM Inconel-718 alloy manufactured by differing island scanning strategy. Opt Laser Technol 2015. https://doi.org/10.1016/j.optlastec.2015.07.009.

[2] Thirugnanasambantham KG, Natarajan S. Degradation mechanism for high temperature erosion in surface modified IN718 superalloy. Surf Eng 2015. https://doi.org/10.1179/1743294414Y.0000000377.

[3] Huang W, Yang J, Yang H, Jing G, Wang Z, Zeng X. Heat treatment of Inconel 718 produced by selective laser melting: microstructure and mechanical properties. Mater Sci Eng 2019. https://doi.org/10.1016/j.msea.2019.02.046.

[4] Gay D. Composite materials: design and applications. third ed. CRC Press; 2014.

[5] Kong D, Dong C, Ni X, Zhang L, Man C, Zhu G, et al. Effect of TiC content on the mechanical and corrosion properties of Inconel 718 alloy fabricated by a high-throughput dual-feed laser metal deposition system. J Alloys Compd 2019. https://doi.org/10.1016/j.jallcom.2019.06.317.

[6] Rui-song J, Wen-hu W, Guo-dong S, Zeng-qiang W. Experimental investigation on machinability of in situ formed TiB2 particles reinforced Al MMCs. J Manuf Process 2016;23:249–57. https://doi.org/10.1016/j.jmapro.2016.05.004.

[7] Hu Q, Zhao H, Li F. Microstructures and properties of SiC particles reinforced aluminum-matrix composites fabricated by vacuum-assisted high pressure die casting. Mater Sci Eng 2017;680:270–7. https://doi.org/10.1016/j.msea.2016.10.090.

[8] Suryanarayana C. Mechanical alloying and milling. Prog Mater Sci 2001. https://doi.org/10.1016/S0079-6425(99)00010-9.

[9] Angelo PC, Subramanian R. Powder metallurgy: science, technology and applications. PHI Learning Pvt. Ltd.; 2008.

[10] Gisario A, Kazarian M, Martina F, Mehrpouya M. Metal additive manufacturing in the commercial aviation industry: a review. J Manuf Syst 2019. https://doi.org/10.1016/j.jmsy.2019.08.005.

[11] Sing SL, Wiria FE, Yeong WY. Selective laser melting of lattice structures: a statistical approach to manufacturability and mechanical behavior. Robot Comput Integr Manuf; 2018. https://doi.org/10.1016/j.rcim.2017.06.006.

[12] Najmon JC, Raeisi S, Tovar A. Review of additive manufacturing technologies and applications in the aerospace industry. Additive Manufacturing for the Aerospace Industry; 2019. https://doi.org/10.1016/b978-0-12-814062-8.00002-9.

[13] Javaid M, Haleem A, Singh RP, Suman R, Rab S. Role of additive manufacturing applications towards environmental sustainability. Adv. Ind. Eng. Polym. Res. 2021;4:312–22. https://doi.org/10.1016/j.aiepr.2021.07.005.

[14] Sun C, Wang Y, McMurtrey MD, Jerred ND, Liou F, Li J. Additive manufacturing for energy: a review. Appl Energy 2021:282. https://doi.org/10.1016/j.apenergy.2020.116041.

[15] AlMangour B, Kim YK, Grzesiak D, Lee KA. Novel TiB2-reinforced 316L stainless steel nanocomposites with excellent room- and high-temperature yield strength developed by additive manufacturing. Compos B Eng 2019;156:51–63. https://doi.org/10.1016/j.compositesb.2018.07.050.

[16] Wen X, Wang Q, Mu Q, Kang N, Sui S, Yang H, et al. Laser solid forming additive manufacturing TiB2 reinforced 2024Al composite: microstructure and mechanical properties. Mater Sci Eng, A 2019;745:319–25. https://doi.org/10.1016/j.msea.2018.12.072.

[17] Liu H, Fang M, Han Y, Huang G, Sun Z, Zhang L, et al. Achieving strength-ductility combination and anisotropy elimination in additively manufactured TiB/Ti6Al4V by in-situ synthesized network architecture with fine grains. Compos B Eng 2023;262:110822. https://doi.org/10.1016/J.COMPOSITESB.2023.110822.

[18] Chen W, Xiao B, Xu L, Han Y, Zhao L, Jing H. Additive manufacturing of martensitic stainless steel matrix composites with simultaneously enhanced strength-ductility and corrosion resistance. Compos B Eng 2022;234:109745. https://doi.org/10.1016/J.COMPOSITESB.2022.109745.

[19] Tan C, Zou J, Wang D, Ma W, Zhou K. Duplex strengthening via SiC addition and in-situ precipitation in additively manufactured composite materials. Compos B Eng 2022;236:109820. https://doi.org/10.1016/J.COMPOSITESB.2022.109820.

[20] Ma C, Ge Q, Yuan L, Gu D, Dai D, Setchi R, et al. The development of laser powder bed fused nano-TiC/NiTi superelastic composites with hierarchically heterogeneous microstructure and considerable tensile recoverable strain. Compos B Eng 2023;250:110457. https://doi.org/10.1016/J.COMPOSITESB.2022.110457.

[21] Borkar T, Gopagoni S, Nag S, Hwang JY, Collins PC, Banerjee R. In situ nitridation of titanium-molybdenum alloys during laser deposition. J Mater Sci 2012;47:7157–66. https://doi.org/10.1007/s10853-012-6656-z.

[22] Tanprayoon D, Srisawadi S, Sato Y, Tsukamoto M, Suga T. Microstructure and hardness response of novel 316L stainless steel composite with TiN addition fabricated by SLM. Opt Laser Technol 2020;129:106238. https://doi.org/10.1016/j.optlastec.2020.106238.

[23] Mandal V, Hussain M, Kumar V, Kumar Das A, Singh NK. Development of reinforced TiN-SS316 metal matrix composite (MMC) using direct Metal laser sintering (DMLS) and its characterization. Mater Today Proc 2017;4:9982–6. https://doi.org/10.1016/j.matpr.2017.06.306.

[24] Zhang S, Chen Z, Wei P, Huang K, Zou Y, Yao S, et al. Microstructure and properties of a nano-ZrO2-reinforced AlSi10Mg matrix composite prepared by selective laser melting. Mater Sci Eng 2022;838:142792. https://doi.org/10.1016/j.msea.2022.142792.

[25] Guo C, Yu Z, Hu X, Li G, Zhou F, Xu Z, et al. Y2O3 nanoparticles decorated IN738LC superalloy manufactured by laser powder bed fusion: cracking inhibition, microstructures and mechanical properties. Compos B Eng 2022;230:109555. https://doi.org/10.1016/J.COMPOSITESB.2021.109555.

[26] Li W, Di R, Yuan R, Song H, Lei J. Microstructure, wear resistance and electrochemical properties of spherical/non-spherical WC reinforced Inconel 625 superalloy by laser melting deposition. J Manuf Process 2022;74:413–22. https://doi.org/10.1016/j.jmapro.2021.12.045.

[27] Marchese G, Aversa A, Bassini E. Microstructure and hardness evolution of solution annealed inconel 625/tic composite processed by laser powder bed fusion. Metals (Basel) 2021;11. https://doi.org/10.3390/met11060929.

[28] Ge T, Chen L, Gu P, Ren X, Chen X. Microstructure and corrosion resistance of TiC/Inconel 625 composite coatings by extreme high speed laser cladding. Opt Laser Technol 2022;150:107919. https://doi.org/10.1016/j.optlastec.2022.107919.

[29] Raahgini C, Verdi D. Abrasive wear performance of laser cladded Inconel 625 based metal matrix composites: effect of the vanadium carbide reinforcement phase content. Surf Coat Technol 2022;429:127975. https://doi.org/10.1016/j.surfcoat.2021.127975.

[30] Zhang B, Bi G, Nai S, Sun CN, Wei J. Microhardness and microstructure evolution of TiB2 reinforced Inconel 625/TiB2 composite produced by selective laser melting. Opt Laser Technol 2016;80:186–95. https://doi.org/10.1016/j.optlastec.2016.01.010.

[31] Zhang B, Bi G, Wang P, Bai J, Chew Y, Nai MS. Microstructure and mechanical properties of Inconel 625/nano-TiB2 composite fabricated by LAAM. Mater Des 2016;111:70–9. https://doi.org/10.1016/j.matdes.2016.08.078.

[32] Zhang Z, Han Q, Yang S, Yin Y, Gao J, Setchi R. Laser powder bed fusion of advanced submicrometer TiB2 reinforced high-performance Ni-based composite. Mater Sci Eng 2021;817:141416. https://doi.org/10.1016/j.msea.2021.141416.

[33] Muvvala G, Patra Karmakar D, Nath AK. In-process detection of microstructural changes in laser cladding of in-situ Inconel 718/TiC metal matrix composite coating. J Alloys Compd 2018;740:545–58. https://doi.org/10.1016/j.jallcom.2017.12.364.

[34] Mandal V, Tripathi P, Kumar A, Singh SS, Ramkumar J. A study on selective laser melting (SLM) of TiC and B4C reinforced IN718 metal matrix composites (MMCs). J Alloys Compd 2022;901:163527. https://doi.org/10.1016/j.jallcom.2021.163527.

[35] Wang Y, Zhuo L, Liu M, An Z, Li C, Yin E, et al. Microstructure characteristics and surface oxidation behaviour of SLM WC/IN718 composite. Powder Metall 2021:1–10. https://doi.org/10.1080/00325899.2021.2014649. 0.

[36] Kim SH, Shin GH, Kim BK, Kim KT, Yang DY, Aranas C, et al. Thermo-mechanical improvement of Inconel 718 using ex situ boron nitride-reinforced composites processed by laser powder bed fusion. Sci Rep 2017;7:1–13. https://doi.org/10.1038/s41598-017-14713-1.

[37] Promakhov V, Matveev A, Klimova-Korsmik O, Schulz N, Bakhmat V, Babaev A, et al. Structure and properties of metal-matrix composites based on an inconel 625–TiB2 system fabricated by additive manufacturing. Metals (Basel) 2022. https://doi.org/10.3390/met12030525.

[38] Zhang Z, Han Q, Liu Z, Wang X, Wang L, Yang X, et al. Influence of the TiB2 content on the processability, microstructure and high-temperature tensile performance of a Ni-based superalloy by laser powder bed fusion. J Alloys Compd 2022;908:164656. https://doi.org/10.1016/J.JALLCOM.2022.164656.

[39] Fahrenholtz WG, Hilmas GE. Oxidation of ultra-high temperature transition metal diboride ceramics. Int Mater Rev 2012. https://doi.org/10.1179/1743280411Y.0000000012.

[40] Fahrenholtz WG, Hilmas GE. Ultra-high temperature ceramics: materials for extreme environments. Scr. Mater. 2017. https://doi.org/10.1016/j.scriptamat.2016.10.018.

[41] Fahrenholtz WG, Hilmas GE, Talmy IG, Zaykoski JA. Refractory diborides of zirconium and hafnium. J Am Ceram Soc 2007. https://doi.org/10.1111/j.1551-2916.2007.01583.x.

[42] Wuchina E, Opila E, Opeka M, Fahrenholtz W, Talmy I. UHTCs: ultra-High Temperature Ceramic materials for extreme environment applications. Electrochemical Society Interface; 2007. https://doi.org/10.1149/2.f04074if.

[43] Neuman EW, Hilmas GE, Fahrenholtz WG. Processing, microstructure, and mechanical properties of large-grained zirconium diboride ceramics. Mater Sci Eng 2016. https://doi.org/10.1016/j.msea.2016.06.017.

[44] Gao Y, Zhang D, Cao M, Chen R, Feng Z, Poprawe R, et al. Effect of δ phase on high temperature mechanical performances of Inconel 718 fabricated with SLM process. Mater Sci Eng, A 2019;767:138327. https://doi.org/10.1016/J.MSEA.2019.138327.

[45] Sui S, Tan H, Chen J, Zhong C, Li Z, Fan W, et al. The influence of Laves phases on the room temperature tensile properties of Inconel 718 fabricated by powder feeding laser additive manufacturing. Acta Mater 2019;164:413–27. https://doi.org/10.1016/J.ACTAMAT.2018.10.032.

[46] Kantzos C, Pauza J, Cunningham R, Narra SP, Beuth J, Rollett A. An Investigation of Process Parameter Modifications on Additively Manufactured Inconel 718 Parts. J Mater Eng Perform n.d.;28. https://doi.org/10.1007/s11665-018-3612-3. .

[47] Zhang D, Niu W, Cao X, Liu Z. Effect of standard heat treatment on the microstructure and mechanical properties of selective laser melting manufactured

Inconel 718 superalloy. Mater Sci Eng, A 2015;644:32–40. https://doi.org/10.1016/J.MSEA.2015.06.021.
[48] Rao GA, Kumar M, Srinivas M, Sarma DS. Effect of standard heat treatment on the microstructure and mechanical properties of hot isostatically pressed superalloy inconel 718. Mater Sci Eng, A 2003;355:114–25. https://doi.org/10.1016/S0921-5093(03)00079-0.
[49] Tekoğlu E, O'Brien AD, Liu J, Wang B, Kavak S, Zhang Y, et al. Strengthening additively manufactured Inconel 718 through in-situ formation of nanocarbides and silicides. Addit Manuf 2023;67:103478. https://doi.org/10.1016/J.ADDMA.2023.103478.
[50] Qu M, Guo Q, Escano LI, Nabaa A, Mohammad S, Hojjatzadeh H, et al. Controlling process instability for defect lean metal additive manufacturing n.d. https://doi.org/10.1038/s41467-022-28649-2..
[51] Du J, Wen B, Melnik R, Kawazoe Y. First-principles studies on structural, mechanical, thermodynamic and electronic properties of Ni–Zr intermetallic compounds. Intermetallics 2014;54:110–9. https://doi.org/10.1016/J.INTERMET.2014.05.021.
[52] Zheng Y, Liu F, Zhang W, Liu F, Huang C, Gao J, et al. The microstructure evolution and precipitation behavior of TiB2/Inconel 718 composites manufactured by selective laser melting. J Manuf Process 2022;79:510–9. https://doi.org/10.1016/J.JMAPRO.2022.04.070.
[53] Zhang Z, Han Q, Yang S, Yin Y, Gao J, Setchi R. Laser powder bed fusion of advanced submicrometer TiB2 reinforced high-performance Ni-based composite. Mater Sci Eng, A 2021;817:141416. https://doi.org/10.1016/j.msea.2021.141416.
[54] Song Z, Gao W, Wang D, Wu Z, Yan M, Huang L, et al. Materials Very-high-cycle fatigue behavior of Inconel 718 alloy fabricated by selective laser melting at elevated temperature. 2021. https://doi.org/10.3390/ma14041001.
[55] Fang XY, Li HQ, Wang M, Li C, Guo YB. Characterization of texture and grain boundary character distributions of selective laser melted Inconel 625 alloy. Mater Char 2018;143:182–90. https://doi.org/10.1016/J.MATCHAR.2018.02.008.
[56] Yao X, Moon SK, Lee BY, Bi G. Effects of heat treatment on microstructures and tensile properties of IN718/TiC nanocomposite fabricated by selective laser melting. Int J Precis Eng Manuf 2017;18:1693–701. https://doi.org/10.1007/s12541-017-0197-y.
[57] Song Q song, Zhang Y, Wei Y feng, Zhou X yi, Shen Y fu, Zhou Y min, et al. Microstructure and mechanical performance of ODS superalloys manufactured by selective laser melting. Opt Laser Technol 2021;144:107423. https://doi.org/10.1016/J.OPTLASTEC.2021.107423.
[58] Sang L, Lu J, Wang J, Ullah R, Sun X, Zhang Y, et al. In-situ SEM study of temperature-dependent tensile behavior of Inconel 718 superalloy. J Mater Sci 2021;56:16097–112. https://doi.org/10.1007/S10853-021-06256-8/FIGURES/12.
[59] Rao GA, Kumar M, Srinivas M, Sarma DS. Effect of standard heat treatment on the microstructure and mechanical properties of hot isostatically pressed superalloy inconel 718. Mater Sci Eng, A 2003;355:114–25. https://doi.org/10.1016/S0921-5093(03)00079-0.
[60] Sun SH, Koizumi Y, Saito T, Yamanaka K, Li YP, Cui Y, et al. Electron beam additive manufacturing of Inconel 718 alloy rods: impact of build direction on microstructure and high-temperature tensile properties. Addit Manuf 2018;23:457–70. https://doi.org/10.1016/J.ADDMA.2018.08.017.
[61] Hart EW. Theory of the tensile test. Acta Metall 1967;15:351–5. https://doi.org/10.1016/0001-6160(67)90211-8.
[62] Hutchinson JW, Neale KW. Influence of strain-rate sensitivity on necking under uniaxial tension. Acta Metall 1977;25:839–46. https://doi.org/10.1016/0001-6160(77)90168-7.
[63] Wang Y, Li J, Hamza AV, Barbee TW. Ductile crystalline-amorphous nanolaminates. Proc Natl Acad Sci U S A 2007;104:11155–60. https://doi.org/10.1073/PNAS.0702344104/SUPPL_FILE/IMAGE1127.GIF.
[64] Huang Z, Abad MD, Ramsey JK, de Figueiredo MR, Kaoumi D, Li N, et al. A high temperature mechanical study on PH 13-8 Mo maraging steel. Mater Sci Eng, A 2016;651:574–82. https://doi.org/10.1016/J.MSEA.2015.10.077.
[65] Misra RDK, Venkatsurya P, Wu KM, Karjalainen LP. Ultrahigh strength martensite–austenite dual-phase steels with ultrafine structure: the response to indentation experiments. Mater Sci Eng A-Struct Mater Propert Microstruct Process 2013;560:693–9. https://doi.org/10.1016/J.MSEA.2012.10.015.
[66] Kontis P, Alabort E, Barba D, Collins DM, Wilkinson AJ, Reed RC. On the role of boron on improving ductility in a new polycrystalline superalloy. Acta Mater 2017;124:489–500. https://doi.org/10.1016/J.ACTAMAT.2016.11.009.
[67] Du J-P, Geng WT, Arakawa K, Li J, Ogata S. Hydrogen-enhanced vacancy diffusion in metals. J Phys Chem Lett 2020;11:7015–20. https://doi.org/10.1021/acs.jpclett.0c01798.
[68] Huang L, Chen D, Xie D, Li S, Zhang Y, Zhu T, et al. Quantitative tests revealing hydrogen-enhanced dislocation motion in α-iron. Nat Mater 2023;22:710–6. https://doi.org/10.1038/s41563-023-01537-w.